ELSEVIER

Contents lists available at ScienceDirect

Magnetic Resonance Imaging

journal homepage: www.elsevier.com/locate/mri





Accelerated multiple-quantum-filtered sodium magnetic resonance imaging using compressed sensing at 7 T

Qingping Chen a,b,1, Wieland A. Worthoff a,*,1,2, N. Jon Shah a,c,d,e

- ^a Institute of Neuroscience and Medicine 4, Forschungszentrum Jülich GmbH, Jülich, Germany
- ^b Faculty of Medicine, RWTH Aachen University, Aachen, Germany
- ^c Institute of Neuroscience and Medicine 11, Forschungszentrum Jülich GmbH, Jülich, Germany
- d JARA-BRAIN-Translational Medicine, Aachen, Germany
- e Department of Neurology, RWTH Aachen University, Aachen, Germany

ARTICLE INFO

Keywords: Multiple quantum filtering Sodium metabolic imaging Enhanced SISTINA Compressed sensing Acquisition time reduction Ultrahigh field

ABSTRACT

Purpose: Multiple-quantum-filtered (MQF) sodium magnetic resonance imaging (MRI), such as enhanced single-quantum and triple-quantum-filtered imaging of ²³Na (eSISTINA), enables images to be weighted towards restricted sodium, a promising biomarker in clinical practice, but often suffers from clinically infeasible acquisition times and low image quality. This study aims to mitigate the above limitation by implementing a novel eSISTINA sequence at 7 T with the application of compressed sensing (CS) to accelerate eSISTINA acquisitions without a noticeable loss of information.

Methods: A novel eSISTINA sequence with a 3D spiral-based sampling scheme was implemented at 7 T for the application of CS. Fully sampled datasets were obtained from one phantom and ten healthy subjects, and were then retrospectively undersampled by various undersampling factors. CS undersampled reconstructions were compared to fully sampled and undersampled nonuniform fast Fourier transform (NUFFT) reconstructions. Reconstruction performance was evaluated based on structural similarity (SSIM), signal-to-noise ratio (SNR), weightings towards total and compartmental sodium, and *in vivo* quantitative estimates.

Results: CS-based phantom and $in\ vivo$ images have less noise and better structural delineation while maintaining the weightings towards total, non-restricted (predominantly extracellular), and restricted (primarily intracellular) sodium. CS generally outperforms NUFFT with a higher SNR and a better SSIM, except for the SSIM in TQ brain images, which is likely due to substantial noise contamination. CS enables $in\ vivo$ quantitative estimates with <15% errors at an undersampling factor of up to two.

Conclusions: Successful implementation of an eSISTINA sequence with an incoherent sampling scheme at 7 T was demonstrated. CS can accelerate eSISTINA by up to twofold at 7 T with reduced noise levels compared to NUFFT, while maintaining major structural information, reasonable weightings towards total and compartmental sodium, and relatively reliable *in vivo* quantification. The associated reduction in acquisition time has the potential to facilitate the clinical applicability of MQF sodium MRI.

1. Introduction

Sodium (²³Na) plays an essential role in cellular metabolic processes through the regulation of the sodium-potassium pump, which maintains a large sodium concentration gradient between the intracellular (typically: 10–15 mmol/l) and extracellular (typically: 140–150 mmol/l) compartments across the cell membrane at the expense of energy [1,2].

Disruption of cell membrane integrity or energy metabolism dysfunction leads to an increased intracellular sodium concentration, whereas the extracellular sodium concentration remains largely unchanged due to tissue perfusion. Therefore, the elevated intracellular sodium caused by abnormal sodium ion homeostasis is often considered a sensitive early indicator of various pathological conditions [1], such as brain tumors [3,4] and multiple sclerosis [5]. Hence, the selective detection of

^{*} Corresponding author.

E-mail address: w.worthoff@fz-juelich.de (W.A. Worthoff).

Qingping Chen and Wieland A. Worthoff should be considered the joint first authors

² Postal address: Institute of Neuroscience and Medicine – 4, Forschungszentrum Jülich GmbH, 52,425 Jülich, Germany

intracellular sodium content is of great interest. However, conventional sodium magnetic resonance imaging (MRI) with a single radiofrequency (RF) pulse only allows the detection of total tissue sodium content. Various advanced approaches have been proposed to monitor the intracellular sodium ions selectively *via* sodium MRI. For example, chemical shift reagents have been used to create a resonance frequency offset for extracellular sodium ions [6], and an inversion recovery technique has been developed for the suppression of sodium signals from an aqueous environment [7].

In addition, multiple-quantum-filtered (MQF) sodium nuclear magnetic resonance (NMR) spectroscopy has been used to monitor intracellular sodium content in animal experiments using the chemical shift reagent technique as a reference [8, 9]. These studies showed that the triple-quantum-filtered (TQ-filtered) sodium signal primarily originated from intracellular sodium ions, whereas the changes in extracellular sodium contents had little effect on the TQ-filtered signal. In light of this, this work applied a multiple-quantum filtering technique for intracellular sodium-weighted imaging, which is proposed as a noninvasive tool to investigate the *in vivo* pathological processes at the cellular level [3,4,10-12]. In recent years, MQF sodium MRI has benefited from the increasing availability of ultrahigh field (7 T or higher) systems, which offer an improved signal-to-noise ratio (SNR), making MQF sodium MRI an enticing technique for clinical practice. However, compared with hydrogen (¹H) MRI, which is widely used in clinical routine, MQF sodium MRI still suffers from the interrelated issues of relatively low image quality and long acquisition times (often exceeding 10 min), hampering its clinical applicability. These issues emerge from the fact that sodium MRI has a relatively low NMR sensitivity of approximately 9.2% compared to hydrogen [13]. The electric quadrupolar nature of the sodium nucleus results in a biexponential transversal relaxation in biological tissues, with a fast component T_{2f}^* (0.5–5 ms) contributing about 60% of the sodium NMR signal and a slow component T_{2s}^* (15–30 ms) corresponding to approximately 40% of the signal [1]. Moreover, highorder sodium coherences suffer from a poor signal intensity, roughly one order of magnitude lower than the signal intensity obtained from conventional total sodium-weighted imaging [14].

Fortunately, compressed sensing (CS) has been shown to accelerate sodium imaging and improve sodium image quality in various studies [15]. CS aids the accurate reconstruction of certain signals or images from raw data sampled below the Nyquist sampling criterion [16,17]. There are three fundamental requirements for applying CS to sodium MRI [18]. First, the image must have a sparse representation in a transform domain so that the noise can be separated and removed from the desired image content. Sodium MRI already fulfills this requirement since sodium images are intrinsically sparse in some transform domains [18,19]. Second, the undersampled k-space data should have low coherence such that the generated artifacts exhibit a noise-like pattern in the image domain and even more so in a properly chosen transform domain. Due to the fast bi-exponential relaxation behavior, sodium MRI typically employs a non-Cartesian ultrashort echo time (UTE) sampling scheme with low coherence (e.g., a radial or spiral acquisition scheme) [15], which is preferred for the application of CS. Third, the desired image should be reconstructed by a nonlinear iterative approach that enforces both the image sparsity in the transform domain and the consistency of the reconstructed image with the measured k-space data. Since Madelin et al. first demonstrated the applicability of CS in sodium MRI in 2012 [19], CS has been used to improve sodium MRI in various anatomical regions, including the human knee [19], brain [20-28], breast [29,30], skeletal muscle [31,32], and human torso [33]. In particular, Blunck et al. investigated the bias in CS-derived estimates in sodium brain MRI and found that CS can accelerate conventional sodium MRI by up to fourfold with good image quality and high total sodium concentration (TSC) quantification accuracy [24]. Furthermore, the clinical potential of CS has been preliminarily demonstrated in multiple pathological conditions, such as ischemic stroke [21,26], multiple

sclerosis [22], and brain tumors [27,34]. However, these studies have only accelerated conventional total sodium-weighted imaging. Intracellular sodium-weighted MQF images are less compressible than total sodium-weighted images due to low image resolution and high noise contamination; therefore, the performance of CS on MQF sodium images is of great interest. To the best of the authors' knowledge, the acceleration of intracellular sodium-weighted MQF sodium MRI by CS, which might potentially be of greater clinical significance, has not yet been investigated.

In this proof-of-concept study, the feasibility of applying CS to accelerate enhanced simultaneous single-quantum (SQ) and TQ-filtered imaging of 23 Na (eSISTINA) [35,36] at 7 T was first investigated. Here, it is assumed that SQ coherences originate from both nonrestricted (mainly extracellular) and restricted (mainly intracellular) environments, whereas TQ coherences develop primarily in a restricted, predominantly intracellular environment only [11]. A novel eSISTINA sequence was developed and implemented using Fermat Looped ORthogonally Encoded Trajectories (FLORET) [37] k-space trajectories with attractive properties, including high sampling efficiency, great SNR retainment for short- T_2^* species, and excellent potential of incoherent undersampling. Fully sampled eSISTINA datasets were obtained from a phantom and ten healthy subjects and retrospectively undersampled over a range of undersampling factors (USFs). Finally, the CS-based images were compared with fully sampled and undersampled images reconstructed by nonuniform fast Fourier transform (NUFFT) to evaluate the effect of CS on image quality, weightings towards total and compartmental sodium, and in vivo quantitative estimates.

2. Material and methods

2.1. eSISTINA sequence implementation

A variation of the eSISTINA sequence was developed and implemented for MQF sodium MRI. As shown in Fig. 1, the novel feature of this sequence is that it employs two sets of 3D spiral-based FLORET kspace trajectories to introduce high incoherence to UTE, SQ, and TQ raw data for CS reconstruction. The eSISTINA sequence has a repetition time (TR) of 150 ms and a total acquisition time of 11 min 10 s. The multiplequantum filter consists of three hard RF pulses separated by a preparation time of $\tau = 9.5$ ms and an evolution time of $\delta = 60$ us. The flip angles are $\alpha_1=\alpha_2=\alpha_3=90^\circ$ and the RF phases are $\varphi_1,\,\varphi_2,$ and φ_3 with the application of an appropriate 12-step phase cycling scheme [36]. The five-echo UTE readout train that takes place during the preparation time provides information on total sodium content and the fast transversal relaxation time, T_{2f}^* . Following the third RF pulse, the six-echo MQF readout train delivers information on multiple quantum coherences and the slow transversal relaxation time, T_{2s}^* . After each readout, the gradient moment is completely rewound to avoid the interference of residual magnetization on high-order coherences. In addition, a spoiler gradient is applied to dephase residual transversal magnetization after the last MQF readout. In this study, two sets of fully sampled FLORET kspace trajectories were calculated and implemented for UTE and MQF readout trains, given user-defined parameters of maximum slew rate, maximum gradient strength, field-of-view (FOV), resolution, and the number of projections. The UTE FLORET (maximum slew rate = 90 mT/ m/ms; maximum gradient strength = 75 mT/m) is composed of 4462 center-out projections with 1 average, whereas the MQF FLORET (maximum slew rate = 5.4 mT/m/ms; maximum gradient strength = 75 mT/m) consists of 372 center-out projections with 12 averages. UTE images were acquired at $TE_{UTE} = \{0.56, 2.41, 4.26, 6.11, 7.96\}$ ms with an 840 Hz/pixel bandwidth, covering an FOV of 320 mm cubic with a nominal resolution of 5 mm cubic and a full width at half maximum (FWHM) of 6.8 mm cubic. SQ and TQ raw data were sampled at TE_{MOF} $= \{10.50, 19.63, 28.76, 37.89, 47.02, 56.15\}$ ms using a readout bandwidth of 130 Hz/pixel, with an FOV of 320 mm cubic, a nominal

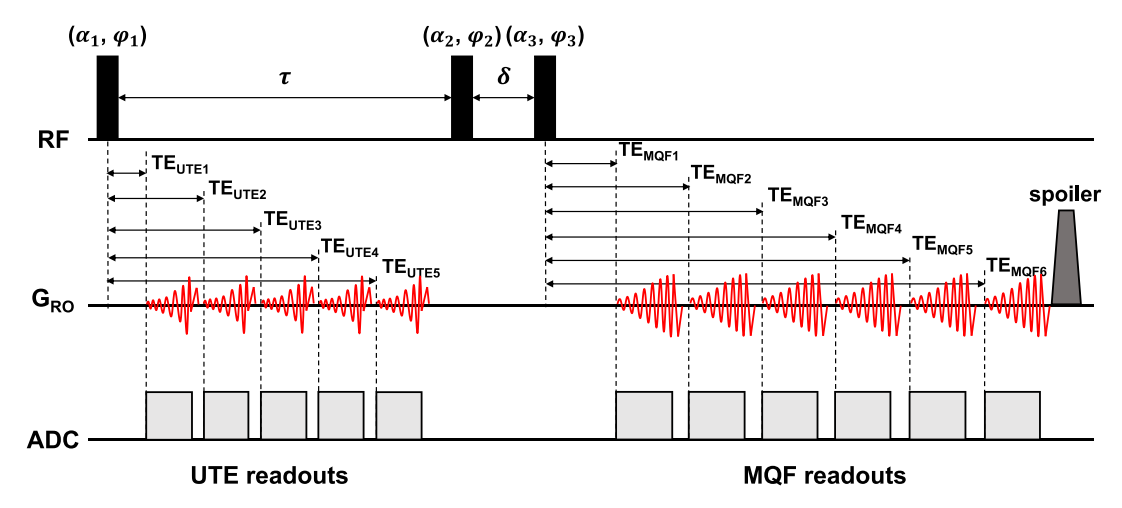


Fig. 1. Diagram of a novel eSISTINA sequence.

This sequence employs two sets of 3D spiral-based FLORET k-space trajectories for the UTE and MQF readout modules (red curves). (For interpretation of the references to colour in this figure legend, the reader is referred to the web version of this article.)

resolution of 10 mm cubic, and an FWHM of 13.7 mm cubic.

2.2. Data acquisition

All MRI images were acquired on a Siemens Terra 7 T MRI scanner (SIEMENS Healthineers, Erlangen, Germany) capable of 80 mT/m maximum gradient amplitude and 200 mT/m/ms maximum slew rate. A single-channel dual-tuned ¹H/²³Na transmit-receive birdcage RF coil (RAPID Biomedical, Germany) was used for hydrogen anatomical imaging and sodium imaging. A cylindrical phantom with a height of 14 cm and a radius of 9 cm (Fig. 3a) was scanned for the validation of the novel eSISTINA sequence. This phantom consists of six compartments with various sodium chloride concentrations of {50, 100, 140} mmol/l and agarose weights per deionized water volume of {0%, 2%, 6%} for the simulation of nonrestricted (compartments 1-2) and variously restricted (compartments 3-6) environments. Brain imaging of ten healthy subjects (3 females, 29.6 \pm 3.8 years of age) was performed to investigate the in vivo performance of the eSISTINA sequence. All human imaging was conducted with the approval of the ethics committee of RWTH Aachen University, Aachen, Germany. Written informed consent was obtained from all subjects before their inclusion in the study. In addition, B₀ shimming, B₀/B₁ field mapping, and hydrogen anatomical imaging were performed during the measurement. The entire measurement took approximately 30 min in the First-Level controlled operating mode.

 B_0 shimming was based on a vendor-supplied 3D shimming routine at the hydrogen Larmor frequency to reduce static field inhomogeneity. The "standard" shimming procedure was performed twice, and the "advanced" shimming procedure was performed three times for optimization. B_0 and B_1 field maps with a resolution of 10 mm cubic were acquired for the correction of SQ/TQ images and were gridded to 5 mm cubic for the correction of UTE images in postprocessing.

Hydrogen anatomical information was obtained to aid in white matter (WM) segmentation of sodium images by utilizing the MP2RAGE [38] sequence with the following parameters: inversion times of 1 s and 3.2 s; 4° flip angles; TR of about 8.2 s; TE of 1.91 ms; GRAPPA factor = 1; FOV = 240 \times 224 \times 144 mm³; resolution = 2 mm cubic; and acquisition time of about 15 min.

2.3. Data undersampling

Prior to image reconstruction, retrospective undersampling was performed on the fully sampled UTE, SQ, and TQ k-space data by

pseudorandomly skipping a subset of projections with five USFs $= \{1.5, 2, 3, 4, 5\}$, leading to reduced numbers of UTE projections $= \{2976, 2232, 1488, 1116, 888\}$, decreased numbers of MQF projections $= \{248, 186, 124, 93, 74\}$, and accelerated acquisition times $= \{447, 335, 224, 168, 134\}$ s. Fig. 2b and i show the FLORET k-spaces of UTE and MQF readouts with original Nyquist sampling, respectively. The variously undersampled UTE and MQF k-spaces are displayed in Fig. 2c-g and j-n, respectively. The pseudorandom undersampling was performed offline in MATLAB 2019a (Mathworks, Natick, MA, USA). This undersampling scheme generates noise-like k-space undersampling artifacts, which are added incoherently to the sparse representation of the FLORET raw data with low coherence. Thus, the described undersampling combined with the FLORET sampling scheme is highly desirable for the application of CS.

2.4. Image reconstruction

The CS reconstruction used in this work adopts a conventional nonlinear iterative algorithm proposed by Lustig et al. [18], formulated as a constrained optimization problem:

$$\widehat{\mathbf{x}} = \operatorname{argmin} \left\{ \|\mathbf{y} - \mathbf{F}_{\mathbf{u}} \mathbf{x}\|_{2}^{2} + \lambda_{1} \|\boldsymbol{\varPsi} \mathbf{x}\|_{1} + \lambda_{2} \mathbf{T} \mathbf{V}(\mathbf{x}) \right\}, \tag{1}$$

where $\| \bullet \|_1$ and $\| \bullet \|_2$ denote the l_1 - and l_2 -norms, respectively; x is the iteratively generated image; \hat{x} is the final reconstructed image; y is the acquired k-space data; F_u is the undersampled NUFFT operator; Ψ is the sparsity transform operator such that Ψx becomes sparse; TV is the finite difference operator to promote image restoration [39]; and λ_1 and λ_2 are the weighting factors of the transform sparsity and finite difference, respectively. The first term ensures data consistency. The second and third terms enforce image sparsity in the transform and finite-difference domains, respectively.

In this study, the minimization problem in Eq. (1) was solved over 320 iterations using a nonlinear conjugate gradient method [18] with a wavelet transform operator, which was shown to outperform the Discrete Cosine Transform operator and Identity operator [24]. The optimal weighting factors, λ_1 and λ_2 , can be different for each data type (UTE, SQ, and TQ); additionally, they might vary slightly across subjects, USFs, and echoes due to differences in raw data. Hence, an empirical search for the best regularization parameters was performed for each reconstruction over a range of weightings: $\lambda_1 = [0, 1.0]$ with a step size of 0.1; for UTE and SQ, $\lambda_2 = \{0, 0.0001, 0.0005, 0.001, 0.005, 0.1, 0.2, 0.3, 0.4, 0.5\}$; and for TQ, $\lambda_2 = \{0, 0.0001, 0.0001, 0.0005, 0.001, 0.0001, 0.0005, 0.001, 0.0001, 0.0005, 0.0001,$

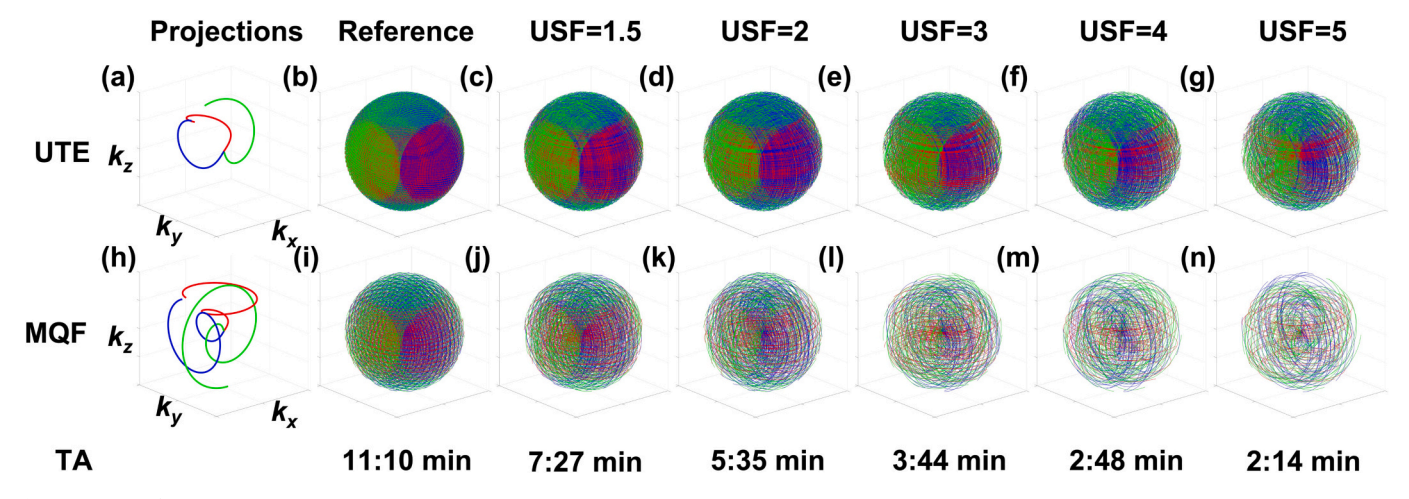


Fig. 2. FLORET k-space trajectories.

Subplots (a) and (h) present the first (red), middle (green), and last (blue) projections of UTE and MQF FLORET, respectively. Fully sampled (b) UTE and (i) MQF FLORET k-spaces were retrospectively undersampled by factors of 1.5, 2, 3, 4, and 5 in a pseudorandom way: undersampled (c-g) UTE and (j-n) MQF k-spaces. TA = total acquisition time. (For interpretation of the references to colour in this figure legend, the reader is referred to the web version of this article.)

0.001, 0.005, 0.01, 0.05, 0.1, 0.2, 0.3, 0.4, 0.5, 0.6, 0.7, 0.8, 0.9, 1.0}. The weighting factors that provided the highest Structural Similarity (SSIM) [40] were chosen.

In addition to CS, NUFFT provided in the Michigan Image Reconstruction Toolbox [41] was used to reconstruct fully sampled and undersampled UTE, SQ, and TQ data. The fully sampled NUFFT-based images were used as references. Each reconstructed image was individually scaled by its maximum intensity to ensure an intensity range from 0 to 1 for image comparison. All reconstructions were performed offline in MATLAB 2019a.

2.5. Image segmentation

Hydrogen WM was extracted from MP2RAGE images and then binarily masked and linearly coregistered to the UTE reference images to obtain UTE WM. The UTE WM mask was then linearly coregistered to SQ reference images to get WM for SQ/TQ data. Hydrogen WM segmentation and linear coregistration were performed in FSL software (FMRIB, Oxford, UK) using the FAST and FLIRT functions, respectively. The resulting partial volume effect maps were thresholded at 0.9, 0.8, and 0.7 to obtain binary WM masks for MP2RAGE, UTE, and SQ/TQ images, respectively. Image segmentation and quantitative analysis (SNR, TSC, $T_{\rm 2T}^{\ast}$, and $T_{\rm 2S}^{\ast}$) were performed on WM only, as gray matter suffers from severe partial volume effects, especially in low-resolution SQ and TQ images. The brain region was manually masked with caution to exclude the skull. The phantom masks were manually determined, and care was taken to avoid partial volume effects.

2.6. Image evaluation

In principle, a reconstruction method should be evaluated based on the diagnostic value of the resulting image; nevertheless, this is not feasible at the proof-of-concept stage. Therefore, the undermentioned methods were used as proxies.

SSIM and SNR were used to evaluate the overall image quality. SSIM measured the structural degradation of an undersampled reconstruction by comparing the test image with the reference image *via* a pixel-wise correlation. SSIM was calculated over a certain region of support (*e.g.*, the whole brain region) to avoid the influence of background noise. SSIM values range from 0 to 1, where a larger SSIM indicates a closer similarity between the test image and the reference image. To obtain an unbiased SNR, the signal amplitude was corrected in all reconstructions

to reduce the effect of noise. The corrected signal, Θ , is given as $\sqrt{\left|\text{mean(signal)}^2 - \sigma_{\text{noise}}^2\right|}$, where σ_{noise} is the standard deviation of the noise distribution assumed to follow a Rayleigh distribution. Noise regions were manually selected from the image background, and caution was taken to exclude the object of interest (e.g., a phantom or a human head). The SNR provided by $\Theta \bullet \sigma_{\text{noise}}^{-1}$ was determined in a specific region of interest (e.g., WM).

Contrasts of total, nonrestricted, and restricted sodium were examined in all reconstructions to investigate whether eSISTINA images maintain the weightings towards total and compartmental sodium after CS-based acceleration. According to the quantum mechanics of eSISTINA [35], UTE images show contrast proportional to total sodium content, independent of the mobility of sodium ions. In addition, since the restricted sodium is more prone to evolve from SQ to TQ coherences under the excitation of a multiple-quantum filter, SQ images are weighted towards nonrestricted sodium; in contrast, TQ images are weighted towards restricted sodium [10].

To investigate the effect of CS on *in vivo* quantitative analysis, the TSC, $T_{2\mathrm{f}}^*$, and $T_{2\mathrm{s}}^*$ of WM in all undersampled reconstructions were calculated and compared with those values obtained from reference reconstructions. The TSC value in WM, TSC_{WM}, was determined using TSC_{WM} = TSC_{ref} • SNR_{WM}/SNR_{ref}, where the SNR of the vitreous humor of the eyes was taken as a reference, SNR_{ref}, with a fixed TSC, TSC_{ref} = 135 mmol/l [42]. SNR_{ref} was calculated based on the top five highintensity voxels in the vitreous humor to reduce partial volume effects. Both SNR_{WM} and SNR_{ref} were obtained from the first-echo UTE images to alleviate signal loss due to relaxation. $T_{2\mathrm{f}}^*$ of WM was determined by UTE fitting given by [36]:

$$SNR_{UTE} = A \bullet exp\left(\frac{TE_{UTE}}{T_{2f}^*}\right) + B \bullet exp\left(\frac{TE_{UTE}}{T_{2,fix}^*}\right), \tag{2}$$

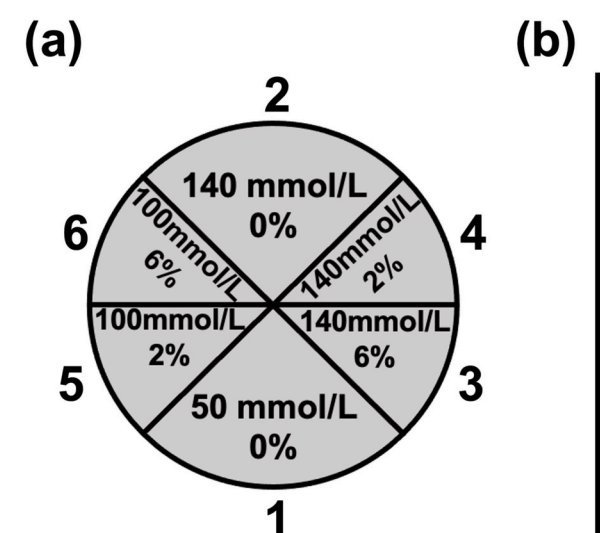
where A and B are constants; $SNR_{\rm UTE}$ and $TE_{\rm UTE}$ are UTE SNR of WM and UTE echo times, respectively. The first term accounts for the fast relaxation component ($T_{\rm 2f}^*$ from restricted sodium). The second term represents the slow relaxation component ($T_{\rm 2s}^*$ from restricted sodium and $T_{\rm 2}^*$ from nonrestricted sodium) and is assumed to have a fixed long relaxation time $T_{\rm 2,fix}^*=35$ ms. The $T_{\rm 2s}^*$ value of WM was obtained from the TQ echo fitting function given by [4]:

$$SNR_{TQ} = C \bullet \left[exp \left(\frac{TE_{MQF}}{T_{2s}^*} \right) - exp \left(\frac{TE_{MQF}}{T_{2s}^*} \right) \right] \bullet \left[exp \left(\frac{\lambda + \tau}{T_{2s}^*} \right) - exp \left(\frac{\lambda + \delta}{T_{2s}^*} \right) \right], \tag{3}$$

where C is a constant; SNR $_{TQ}$ and TE_{MQF} are the TQ SNR of WM and MQF echo times, respectively; $\lambda=1$ ms is the RF pulse duration; $\tau=9.5$ ms is the preparation time, and $\delta=60$ us is the evaluation time. T_{2f}^* is the value obtained from UTE fitting in Eq. (2). If UTE fitting was unreliable (i.e., the fitting error was >50%) or if the fit did not converge, Eq. (3) was used to obtain both T_{2f}^* and T_{2s}^* values [4]. In the UTE and TQ fittings described above, the unbiased SNR serves as a proxy of the signal from the region of interest.

Statistical analysis was used to evaluate the *in vivo* performance of CS. The paired right-tailed Student's *t*-test was applied to compare SNR and SSIM between NUFFT and CS undersampled reconstructions over ten healthy subjects. The Wilcoxon right-tailed rank sum test was used if SNR or SSIM did not follow a normal distribution and was checked by the Lilliefors test. A *p*-value of 0.05 or less was considered significant.

Descriptive statistics for all quantitative parameters, including TSC, $T_{2\mathrm{f}}^*$, and $T_{2\mathrm{s}}^*$, were provided as means and standard deviations for all subjects. Given that quantitative estimates are relatively sensitive to image intensity elevation caused by excessive smoothing in CS reconstructions, *in vivo* quantitative performance was assessed by calculating the mean difference in quantitative values between test and reference reconstructions across all subjects. For example, the mean difference (in %) in TSC from CS is given by $\Delta = \frac{\sum_{i=1}^{10} \left[\left(\mathrm{TSC}_{\mathrm{CS},i} - \mathrm{TSC}_{\mathrm{ref}} \right) / \mathrm{TSC}_{\mathrm{ref}} \right]}{10}$, where TSC_{CS,i} and TSC_{ref} are the TSC values of the *i*th subject obtained from CS and reference reconstructions, respectively. The quantification of the test reconstruction was considered relatively reliable if the absolute mean differences of all quantitative estimates were <15%.



Phantom with 6 compartments

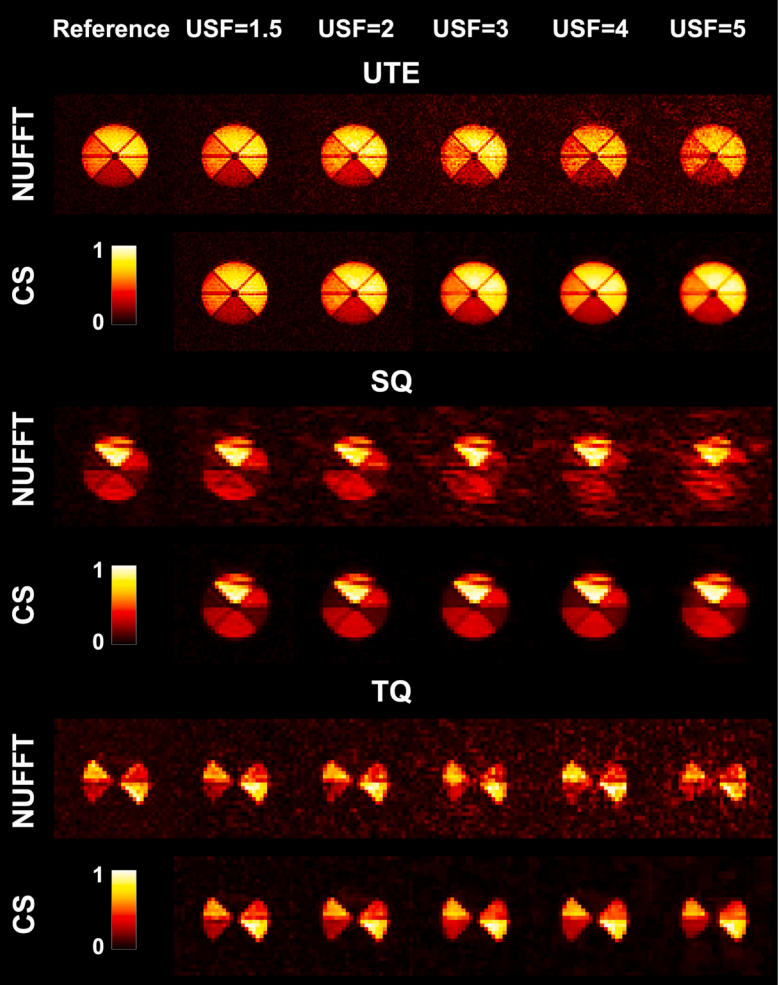


Fig. 3. Schematic and first-echo eSISTINA images of a phantom.

(a) The schematic shows sodium chloride concentration in mmol/l and agarose weight/deionized water volume in percent (e.g., 2% indicates 2 g of agarose powder per 100 ml deionized water). (b) Comparison of NUFFT and CS across all USFs on the first-echo eSISTINA images of the phantom. The UTE (5 mm cubic), SQ (10 mm cubic), and TQ (10 mm cubic) datasets were acquired at the Nyquist sampling rate and retrospectively undersampled by factors of 1.5, 2, 3, 4, and 5. The original, fully sampled images reconstructed by NUFFT were set as references.

3. Results

3.1. Phantom results

The NUFFT and CS reconstructions of the first-echo UTE, SQ, and TQ data from a sodium agarose phantom (Fig. 3a) with various USFs are displayed in Fig. 3b. In the case of undersampling, CS generally outperforms NUFFT, with noticeably reduced noise levels and overall better preservation of structural information present in the reference images. Moreover, the CS-based SQ/TQ images, as well as CS-based UTE images with high USFs, even show less noise than the corresponding reference images. However, more blurring appears in CS-based images with increasing USF, which may lead to a loss of contrast and information.

As shown in Fig. 3b, for all NUFFT and CS reconstructions, UTE images exhibit contrast proportional to the sodium concentration, regardless of the agarose percentage, whereas SQ and TQ images present contrast dependent on the agarose concentration: at the same sodium molarity, SQ signal intensities decrease, and yet TQ signal intensities increase with increasing agarose concentration. Moreover, the signal of

sodium liquids simulating a nonrestricted environment is well suppressed in TQ images. These observations are in good agreement with the quantum mechanics of eSISTINA [35].

Fig. 4 shows the quantitative image quality measures of CS and NUFFT reconstructions of the phantom data across all USFs and all echoes. In various cases of undersampling, CS yields better SSIM and SNR than NUFFT, except that 4 CS-based SQ/TQ SSIM values are marginally lower than those from NUFFT but still show relatively high values of about 0.9. Moreover, the CS-based SNR values are even higher than the reference values in most reconstructions, especially for SQ and TQ images. In CS, SNR shows an upward trend while SSIM decreases slightly with increasing USF, possibly due to the blurring and loss of small structures caused by strong undersampling.

3.2. In vivo results

NUFFT and CS reconstructions of a representative *in vivo* dataset with multiple USFs are shown in Fig. 5. From visual inspection, CS generally leads to remarkedly reduced noise levels and better delineation of brain

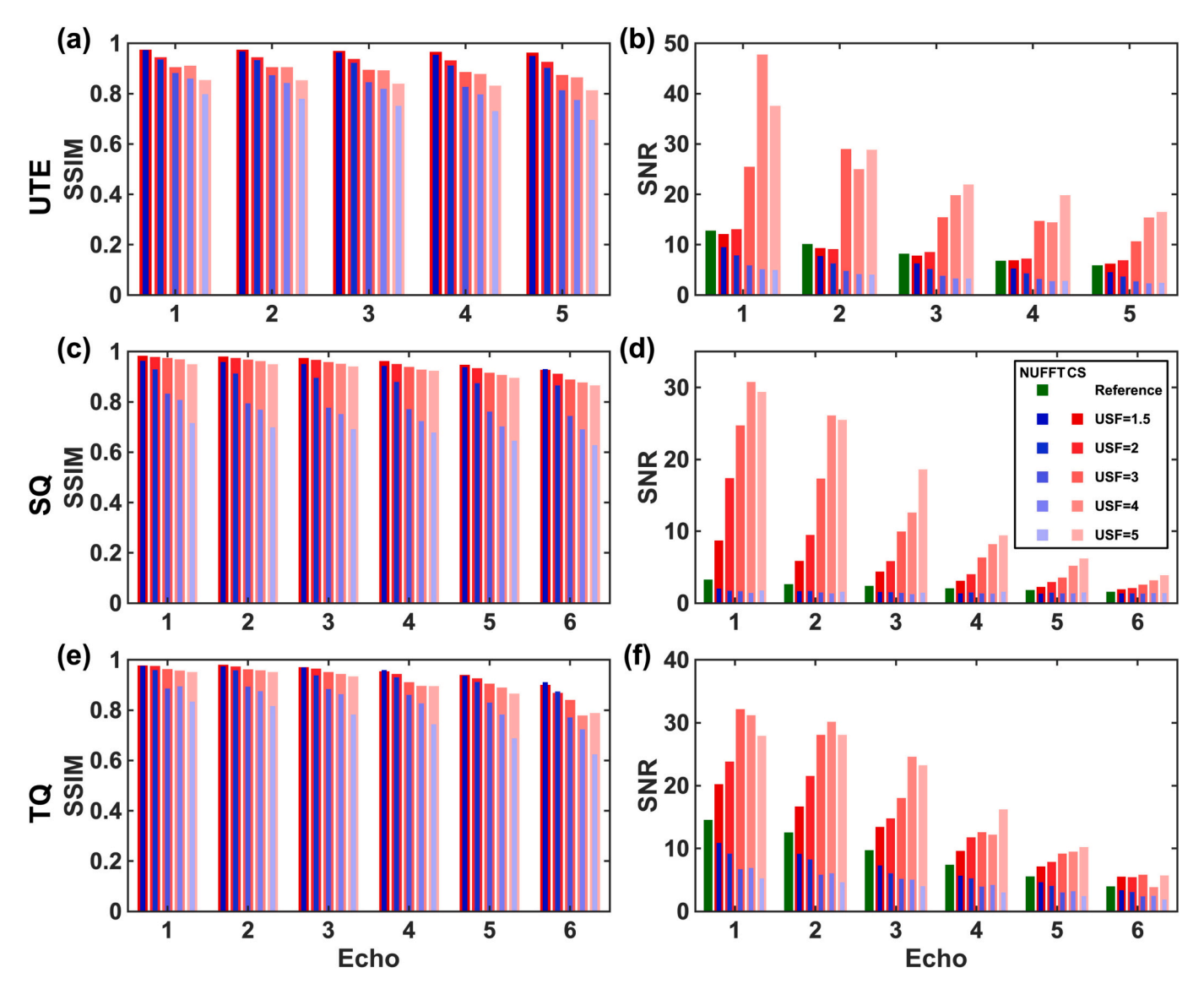


Fig. 4. Image quality measures of NUFFT and CS reconstructions of phantom (Fig. 3a) data across all USFs and all echoes.

The NUFFT-based full sampling was used as a reference (green). The values obtained from NUFFT (blue) and CS (red) reconstructions with different USFs are represented by different colour gradients. SSIM was calculated over the whole phantom for (a) UTE (5 mm cubic) and (c) SQ (10 mm cubic) images, and over the phantom compartments 3–6 for (e) TQ (10 mm cubic) images. SNR was calculated over the phantom compartment 6 for (b) UTE, (d) SQ, and (f) TQ images. The legend in subplot d applies to all subplots. (For interpretation of the references to colour in this figure legend, the reader is referred to the web version of this article.)

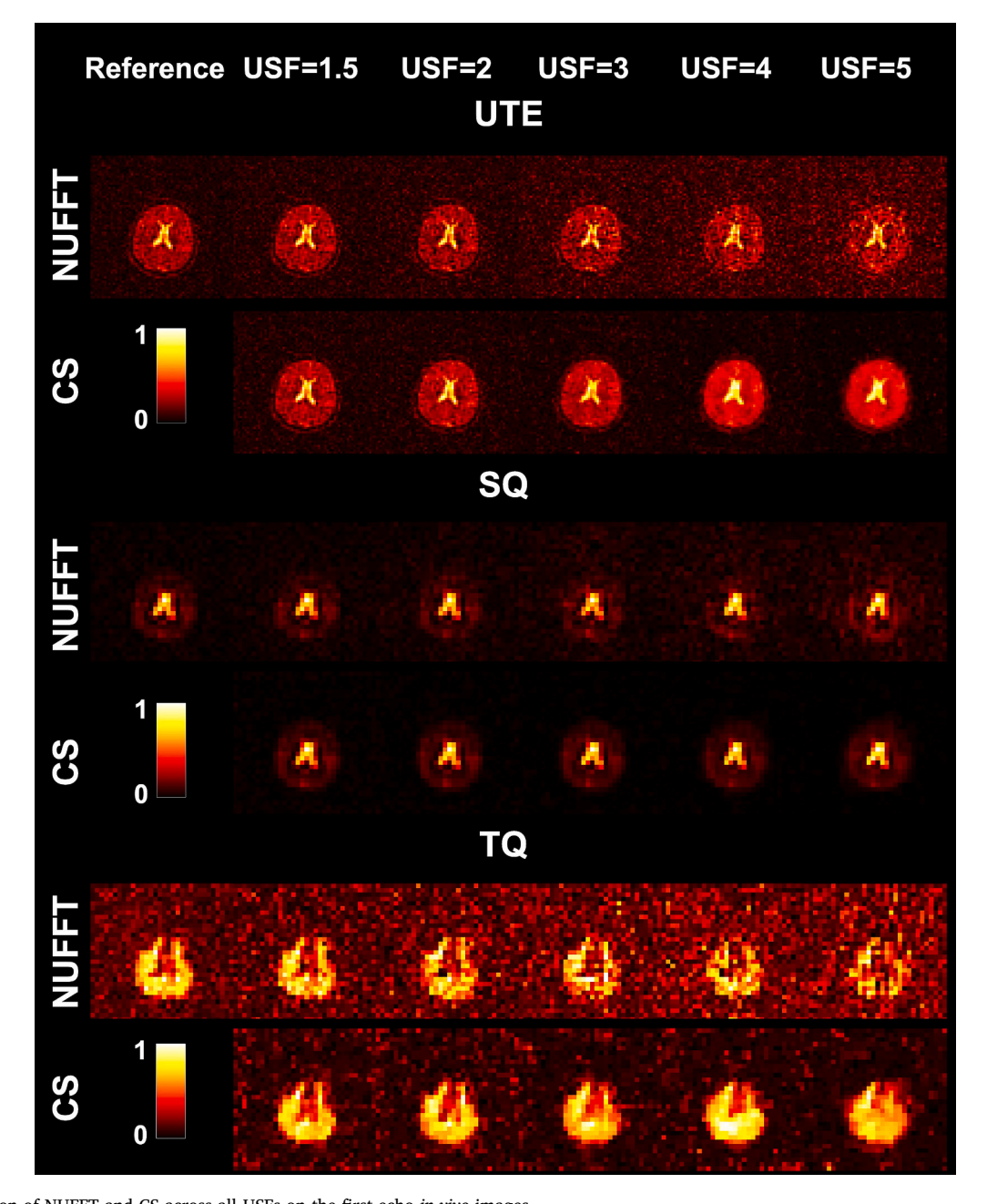


Fig. 5. Comparison of NUFFT and CS across all USFs on the first-echo *in vivo* images.

The UTE (5 mm cubic), SQ (10 mm cubic), and TQ (10 mm cubic) datasets were acquired from the brain of a 32-year-old healthy female subject at the Nyquist sampling rate and retrospectively undersampled by factors of 1.5, 2, 3, 4, and 5. The original, fully sampled images reconstructed by NUFFT are presented as references.

structures compared to NUFFT at various USFs. It should be noted that the information contained in the TQ reference image may be biased by strong noise contamination, which makes it difficult to compare the undersampled TQ image with the TQ reference image. In the case of high USFs (e.g., USF = 4 or 5), even large structures like the gray matter are hardly visible in NUFFT due to substantial noise, whereas the gray matter can be reliably delimited in CS. However, a loss of contrast and information caused by excessive smoothing can be observed in CS reconstructions with high undersampling.

As shown in Fig. 5, the CSF region with high sodium concentration appears bright in all UTE and SQ images, as expected. Conversely, the signal from the CSF area with a nonrestricted environment is well suppressed in all TQ images. Additionally, the brain tissues composed of gray matter and WM, which provide both nonrestricted and restricted

environments, yield higher signal intensity than the CSF area in all TQ images despite the relatively low tissue sodium concentration [1]. The weightings towards total, nonrestricted, and restricted sodium in all *in vivo* images align with those in the phantom images in Fig. 3b.

The reconstructions of data from other echoes and other volunteers yield similar results. Fig. 6 shows the evaluation of the reconstruction performance of NUFFT and CS over a group of ten healthy subjects across all USFs and all echoes using SSIM and SNR. CS yields significantly (p < 0.05) higher SNR values than NUFFT in UTE, SQ, and TQ images for all echoes and all USFs (Fig. 6b, d, f). Moreover, the CS-based SNR values are better than the reference values in most cases. With increasing USF, the NUFFT-based SNR is reduced due to undersampling, whereas the CS-based SNR rises because CS tends to excessive smoothing at high USFs. As shown in Fig. 6a and c, in both UTE and SQ images, CS

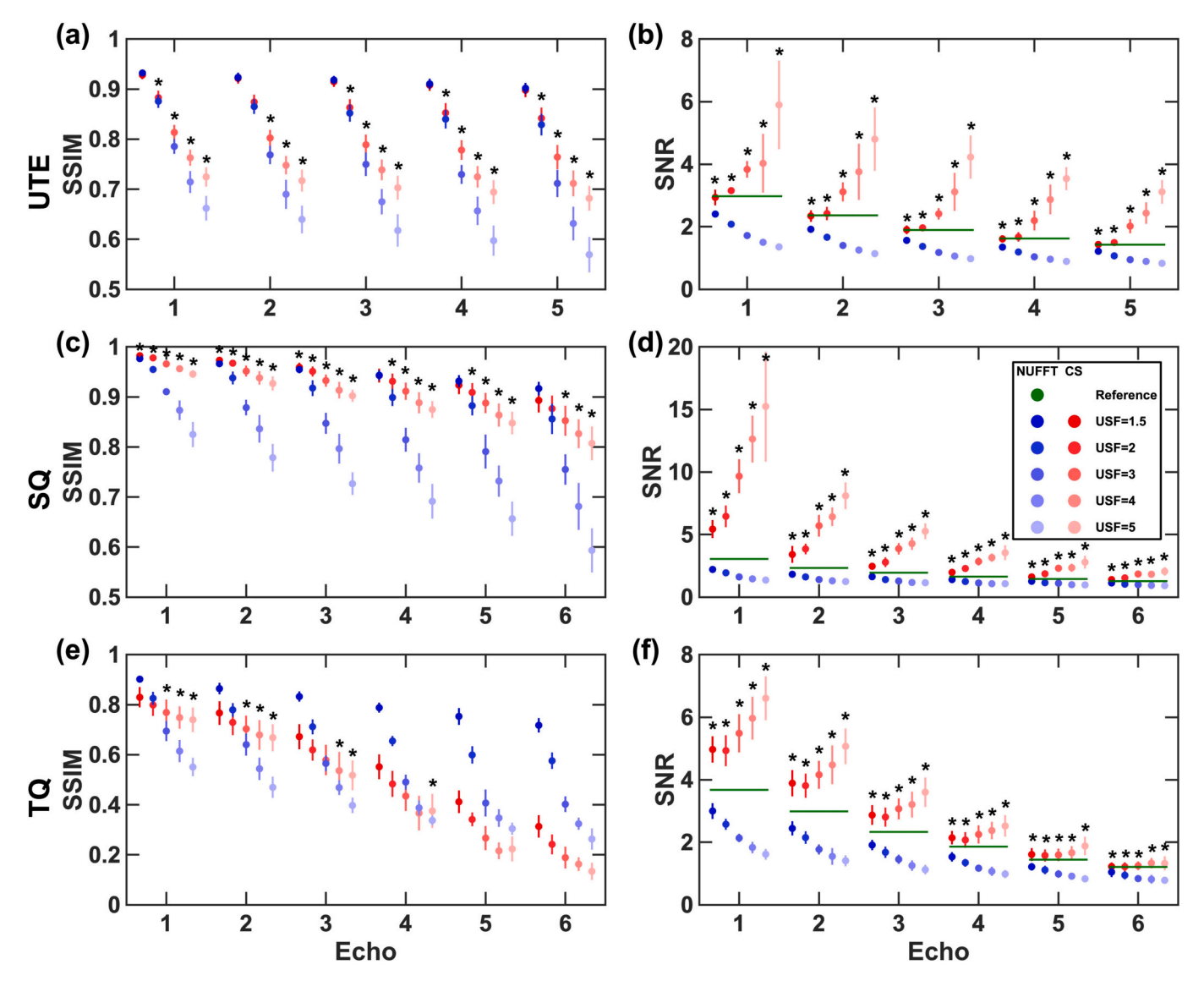


Fig. 6. Image quality measures of NUFFT and CS reconstructions of $in\ vivo$ data from ten healthy subjects across all USFs and all echoes. SSIM and SNR values were obtained from reference (green), NUFFT undersampled (blue), and CS undersampled (red) reconstructions. The means and standard deviations of SSIM and SNR over ten healthy subjects are represented by dots and whiskers, respectively. SSIM (a, c, e) and SNR (b, d, f) were calculated over the whole brain region and the white matter area, respectively. An asterisk (*) is marked when the CS-based SSIM or SNR values are significantly (p < 0.05) higher than those from NUFFT. The legend in subplot d applies to all subplots. (For interpretation of the references to colour in this figure legend, the reader is referred to the web version of this article.)

 Table 1

 Summary statistics of quantitative analysis of ten healthy subjects.

		Reference	USF = 1.5	USF = 2	USF = 3	USF = 4	USF = 5
T _{2f} (ms)	NUFFT	4.8 ± 0.3	$4.5 \pm 0.4 (-5\%)$	$4.3 \pm 0.4 (-9\%)$	$4.3 \pm 0.5 (-8\%)$	$4.1 \pm 0.5 (-14\%)$	4.1 ± 0.5 (-14%)
	CS	_	$4.3 \pm 1.4 (-10\%)$	$4.1 \pm 1.2 (-13\%)$	$3.2 \pm 1.1 \; (-34\%)$	$3.3 \pm 1.7 \ (-32\%)$	$3.3 \pm 1.6 \ (-31\%)$
T _{2s} (ms)	NUFFT	29.9 ± 2.0	36.6 ± 2.9 (22%)	$38.7 \pm 2.8 \ (30\%)$	$43.4 \pm 3.9 (46\%)$	$43.5 \pm 3.6 \ (46\%)$	$44.9 \pm 4.1 \ (51\%)$
	CS	_	$28.6 \pm 3.3 (-4\%)$	$27.8 \pm 3.3 (-7\%)$	$28.9 \pm 2.3 (-2\%)$	$28.3 \pm 3.0 (-3\%)$	$28.3 \pm 3.6 (-5\%)$
TSC (mmol/l)	NUFFT	41.9 ± 1.2	$42.0 \pm 1.2 (0\%)$	$41.6 \pm 1.8 (-1\%)$	$42.1 \pm 1.1 (1\%)$	$41.4 \pm 1.8 (-1\%)$	$41.0 \pm 2.3 (-2\%)$
	CS	-	$41.9 \pm 1.2 (0\%)$	$43.7 \pm 1.7 (4\%)$	$47.9 \pm 0.8 (15\%)$	52.8 ± 1.5 (26%)	54.1 ± 2.3 (29%)

Abbreviations: USF = undersampling factor, NUFFT = non-uniform fast Fourier transform, CS = compressed sensing, $T_{2\mathrm{f}}^*$ = fast transversal relaxation time, $T_{2\mathrm{s}}^*$ = slow transversal relaxation time, TSC = total sodium concentration.

The quantitative parameters, T_{2f}^* , T_{2s}^* , and TSC, obtained from NUFFT-based full sampling, are presented as reference values. The quantitative values obtained from NUFFT and CS undersampled reconstructions by factors of 1.5, 2, 3, 4, and 5 are compared to the reference values. Values in the form of mean \pm std. represent the means and standard deviations of quantitative parameters over ten healthy subjects. The mean difference between the quantitative estimate and the reference value across ten subjects is given in parentheses. Differences that fall within the range from -15% to 15% are marked in bold.

leads to SSIM values significantly better than NUFFT, except for a few cases where CS-based SSIM is only comparable to NUFFT-based SSIM but still has a sufficiently high value of about 0.9. However, in TQ images, most CS reconstructions result in similar or even worse SSIM values compared with NUFFT (Fig. 6e), although from visual inspection, CS generally outperforms NUFFT with better preservation of the primary structural information present in the TQ reference image for all USFs (Fig. 5). As USF increases, both NUFFT-based and CS-based SSIM values decrease, but CS-based SSIM drops more slowly than NUFFT-based SSIM due to the denoising nature of CS.

Table 1 presents the summary statistics for the quantitative analysis on a group of ten healthy subjects. The reference values for WM obtained from original, fully sampled NUFFT-based reconstructions are $T_{2\mathrm{f}}^*=4.8$

 \pm 0.3 ms, $T_{2\rm s}^*=29.9\pm2.0$ ms, and TSC $=41.9\pm1.2$ mmol/l. These values are comparable to the literature values with $T_{2\rm f}^*$ from 0.5 ms to 5 ms, $T_{2\rm s}^*$ from 15 ms to 30 ms, and TSC of 43 \pm 3 mmol/l [5,43]. NUFFT yields <15% bias in both $T_{2\rm f}^*$ and TSC for all USFs, whereas quantification of $T_{2\rm f}^*$ and TSC using CS is only reliable at low USFs. However, it is remarkable that for all USFs, the CS-based $T_{2\rm s}^*$ values compare well with the reference values, whereas the NUFFT-based $T_{2\rm s}^*$ values are overestimated with a mean difference larger than 15%.

4. Discussion

Motivated by the fact that MQF sodium MRI suffers from clinically infeasible measurement times and low image quality, this work implements a novel eSISTINA sequence with an incoherent sampling scheme at 7 T and demonstrates that CS can be applied to reconstruct moderately undersampled eSISTINA data without noticeably degrading the performance of the sequence.

In this study, CS has three advantages that are especially desirable for accelerated eSISTINA. First, CS can improve the image quality of undersampled eSISTINA images with substantial noise suppression and sound structural information recovery. In various cases of undersampling, the visual performance of CS was superior to NUFFT, with notably reduced noise levels in both phantom (Fig. 3) and in vivo (Fig. 5) measurements, which was confirmed by SNR measures (Figs. 4b, d, f and 6b, d, f). Most CS undersampled reconstructions yielded SNR values even higher than fully sampled reference reconstructions. The considerable noise reduction facilitated the delineation of structures in CS, whereas these structures were difficult to distinguish from the substantial noise contamination in NUFFT. Consequently, CS generally outperformed NUFFT in the SSIM measures of phantom (Fig. 4a, c, e) and in vivo (Fig. 6a, c) images, with the exception of TQ brain images (Fig. 6e). One possible explanation for the inferior in vivo performance of TQ SSIM is that severe noise contamination in TQ brain images may produce biased estimates of SSIM and, in particular, here the CS-based SSIM was underestimated by comparing greatly denoised CS-based brain images with heavily noisy TO reference brain images.

The second advantage of CS is that it had little effect on the weightings towards total, nonrestricted, and restricted sodium in eSIS-TINA images from both phantom (Fig. 3) and *in vivo* (Fig. 5) studies. This suggests that with CS-based acceleration, the eSISTINA sequence can still maintain its performance in yielding a weighting towards total sodium in UTE images, a weighting towards nonrestricted sodium in SQ images, and a weighting towards restricted sodium in TQ images.

Third, CS enabled relatively reliable quantification of $T_{2\mathrm{f}}^*$, $T_{2\mathrm{s}}^*$, and TSC values with a USF of up to two, whereas NUFFT failed in the quantification due to the overestimation of $T_{2\mathrm{s}}^*$ value (Table 1). A possible explanation for the overestimated $T_{2\mathrm{s}}^*$ is that the SNR values taken from undersampled NUFFT-based TQ images were too low for the signal decay fitting routine to obtain accurate $T_{2\mathrm{s}}^*$.

Despite the above advantages, there are three practical limitations

and considerations when applying CS to MQF sodium MRI. First, there is no gold standard for SNR and structure preservation measures in nonlinear iterative reconstructions, making it difficult to compare different algorithms. Common approaches for determining SNR depend on a spatially uniform noise distribution with known statistical characteristics; for example, the method used in this study requires a Rayleigh noise distribution. Unlike NUFFT-based noise profiles adequately described by the Rayleigh distribution, the spatial and statistical properties of noise from iterative reconstructions remain unclear. This may bias the estimation of SNR values (Figs. 4b, d, f and 6b, d, f) and other relative parameters, such as T_{2f}^* , T_{2s}^* , and TSC in CS reconstructions (Table 1). SSIM was chosen to measure structural information degradation but is only meaningful if the ground truth image is known. Given that ground truth images were unavailable in this study, reference images were used as an alternative for computing SSIM. This may lead to unreliable SSIM values if the reference image does not agree well with the ground truth, such as the TO reference brain image being heavily contaminated by noise (Figs. 5, 6e). The structural degradation could be better analyzed by computing the local point spread function [44]. However, it cannot be directly applied to non-Cartesian FLORET data since the image reconstruction involves gridding interpolation.

The second limitation is the long reconstruction times and difficult parameterization of CS. CS requires complex iterative algorithms to solve nonlinear optimization problems, leading to long processing times (usually hours). In addition, manual tuning of regularization parameters was performed for each reconstruction task in this study, which resulted in a heavy computational burden. It was observed that CS exhibited poor generalization across data types but good generalization across subjects, echoes, and USFs. Thus, the regularization parameters, λ_1 and λ_2 , can be kept constant for different subjects, echoes, and USFs to reduce the computational burden. Moreover, the reconstruction performance of CS is sensitive to parameter tuning. The rigid manual tuning using empirical search in this study may have led to image quality dispersion among different subjects and echoes, which may have biased the TSC estimate and echo fitting for $T_{2\rm f}^*$ and $T_{2\rm s}^*$. Fortunately, deep learning has been shown to enable fast and accurate reconstruction of undersampled kspace data without manual parameter tuning and could be applied to mitigate this limitation in future work [26,45].

Third, the noise level decreased with increasing USF (Figs. 4b, d, f and 6b, d, f), while the errors in image contrast (Figs. 4a, c, e and 6a, c, e) and quantitative analysis (Table 1) increased. Hence, consideration must be given to selecting an appropriate USF that balances these two factors. In this work, CS only enabled a USF of up to two for eSISTINA, with reduced noise levels and proper maintenance of visual information and quantitative estimates. The achievable USF in non-hydrogen MRI is limited compared with hydrogen MRI, which is mainly due to the intense noise caused by the relatively low NMR sensitivity of non-hydrogen nuclei. Previous studies have shown that the performance of conventional CS in sodium MRI can be further improved by incorporating hydrogen anatomical constraints [20,22,27] or sparsity in learned dictionaries [23,25,28]. Furthermore, supplying prior knowledge about temporal signal evolution led to a more accurate estimation of transversal relaxation times for CS in hydrogen MRI [46]. The above constraints could be added to the CS cost function shown in Eq. (1), which may enable a higher USF for MQF sodium MRI.

In the future, the clinical potential of CS-based accelerated MQF sodium MRI may be investigated in several areas. For example, given that the resolution of conventional eSISTINA images is commonly sacrificed for shorter measurement times and higher SNR, applying CS to achieve higher-resolution MQF sodium imaging while maintaining an acceptable protocol duration has the potential to yield an important clinical impact.

Since the intracellular sodium concentration, volume fraction, and molar fraction can further provide valuable information for diagnosis or medical treatment [3,4,36], it is worth investigating the effect of CS on

intracellular sodium quantification.

Furthermore, CS is not limited to sodium MRI but can also be applied to other nuclei with even lower NMR sensitivity, such as potassium (³⁹K), chlorine (³⁵Cl), and oxygen (¹⁷O) [47].

5. Conclusions

Driven by the interest in a reduction in acquisition time for MQF sodium MRI, this proof-of-concept study establishes a novel eSISTINA sequence with an incoherent sampling scheme at 7 T and demonstrates the feasibility of applying CS to accelerate eSISTINA acquisitions of the human brain. The experimental results on retrospectively undersampled k-space data show that CS can accelerate eSISTINA by up to a factor of two at 7 T with higher SNR and better structural preservation than NUFFT, while maintaining relatively reliable *in vivo* quantification and proper weightings towards total and compartmental sodium. The feasibility of sequence implementation and the reduction in acquisition times have the potential to facilitate the applicability of MQF sodium MRI in clinical practice.

CRediT authorship contribution statement

Qingping Chen: Methodology, Software, Validation, Formal analysis, Investigation, Writing – original draft, Writing – review & editing, Visualization. Wieland A. Worthoff: Conceptualization, Methodology, Software, Investigation, Resources, Data curation, Writing – original draft, Writing – review & editing, Supervision, Project administration. N. Jon Shah: Conceptualization, Resources, Data curation, Writing – review & editing, Supervision, Project administration, Funding acquisition.

Declaration of competing interest

None.

Acknowledgments

The authors thank Anita Köth, Claire Rick, Cindy Roß, Elke Bechholz, Petra Engels, and Wilma Fladung for their kind support. Qingping Chen was funded *via* the Jülich – University of Melbourne Postgraduate Academy (JUMPA). This work is considered to be part of the doctoral thesis (Dr. rer. Medic.) of Qingping Chen at Faculty of Medicine, RWTH Aachen University, Germany.

References

- [1] Madelin G, Lee J-S, Regatte RR, Jerschow A. Sodium MRI: methods and applications. Prog Nucl Magn Reson Spectrosc 2014;79:14–47. https://doi.org/ 10.1016/j.pnmrs.2014.02.001.
- [2] Rose AM, Valdes R. Understanding the sodium pump and its relevance to disease. Clin Chem 1994;40:1674–85. https://doi.org/10.1093/clinchem/40.9.1674.
- [3] Shymanskaya A, Worthoff WA, Stoffels G, Lindemeyer J, Neumaier B, Lohmann P, et al. Comparison of [18F]Fluoroethyltyrosine PET and sodium MRI in cerebral gliomas: a pilot study. Mol Imaging Biol 2020;22:198–207. https://doi.org/10.1007/s11307-019-01349-y.
- [4] Worthoff WA, Shymanskaya A, Lindemeyer J, Langen KJ, Shah NJ. Relaxometry and quantification in sodium MRI of cerebral gliomas: a FET-PET and MRI smallscale study. NMR Biomed 2020;33:e4361. https://doi.org/10.1002/nbm.4361.
- [5] Inglese M, Madelin G, Oesingmann N, Babb JS, Wu W, Stoeckel B, et al. Brain tissue sodium concentration in multiple sclerosis: a sodium imaging study at 3 tesla. Brain A J Neurol 2010;133:847–57. https://doi.org/10.1093/brain/awp334.
- [6] Winter PM, Seshan V, Makos JD, Sherry AD, Malloy CR, Bansal N. Quantitation of intracellular [Na+] in vivo by using TmDOTP5- as an NMR shift reagent and extracellular marker. J Appl Physiol 1998;85:1806–12. https://doi.org/10.1152/ jappl.1998.85.5.1806.
- [7] Nagel AM, Amarteifio E, Lehmann-Horn F, Jurkat-Rott K, Semmler W, Schad LR, et al. 3 tesla sodium inversion recovery magnetic resonance imaging allows for improved visualization of intracellular sodium content changes in muscular channelopathies. Invest Radiol 2011;46:759–66. https://doi.org/10.1097/RIJ.0b013e31822836f6.
- [8] Tauskela JS, Dizon JM, Whang J, Katz J. Evaluation of multiple-quantum-filtered 23Na NMR in monitoring intracellular Na content in the isolated perfused rat heart

- in the absence of a chemical-shift reagent. J Magn Reson 1997;127:115–27. https://doi.org/10.1006/jmre.1997.1181.
- [9] Seshan V, Sherry AD, Bansal N. Evaluation of triple quantum-filtered 23Na NMR spectroscopy in the in situ rat liver. Magn Reson Med 1997;38:821–7. https://doi. org/10.1002/mrm.1910380519.
- [10] Jaccard G, Wimperis S, Bodenhausen G. Multiple-quantum NMR spectroscopy of S=3/2 spins in isotropic phase: a new probe for multiexponential relaxation. J Chem Phys 1986;85:6282–93. https://doi.org/10.1063/1.451458.
- [11] Rooney WD, Springer CSJ. A comprehensive approach to the analysis and interpretation of the resonances of spins 3/2 from living systems. NMR Biomed 1991;4:209–26. https://doi.org/10.1002/nbm.1940040502.
- [12] Choi CH, Stegmayr C, Shymanskaya A, Worthoff WA, da Silva NA, Felder J, et al. An in vivo multimodal feasibility study in a rat brain tumour model using flexible multinuclear MR and PET systems. EJNMMI Phys 2020;7:50. https://doi.org/ 10.1186/s40658-020-00319-6.
- [13] Boada FE, LaVerde G, Jungreis C, Nemoto E, Tanase C, Hancu I. Loss of cell ion homeostasis and cell viability in the brain: what sodium MRI can tell us. Curr Top Dev Biol 2005;70:77–101. https://doi.org/10.1016/S0070-2153(05)70004-1.
- [14] Benkhedah N, Bachert P, Semmler W, Nagel AM. Three-dimensional biexponential weighted 23Na imaging of the human brain with higher SNR and shorter acquisition time. Magn Reson Med 2013;70:754–65. https://doi.org/10.1002/ mrm.24516.
- [15] Chen Q, Shah NJ, Worthoff WA. Compressed sensing in sodium magnetic resonance imaging: techniques, applications, and future prospects. J Magn Reson Imaging 2022;55:1340–56. https://doi.org/10.1002/jmri.28029.
- [16] Donoho DL. Compress Sens IEEE Trans Inf Theory 2006;52:1289–306. https://doi. org/10.1109/TTT.2006.871582.
- [17] Candès EJ, Romberg JK, Tao T. Stable signal recovery from incomplete and inaccurate measurements. Commun Pure Appl Math 2006;59:1207–23. https:// doi.org/10.48550/arXiv.math/0503066.
- [18] Lustig M, Donoho D, Pauly JM. Sparse MRI: the application of compressed sensing for rapid MR imaging. Magn Reson Med 2007;58:1182–95. https://doi.org/ 10.1002/mrm.21391.
- [19] Madelin G, Chang G, Otazo R, Jerschow A, Regatte RR. Compressed sensing sodium MRI of cartilage at 7T: Prepiminary study. J Magn Reson 2012;214:360–5. https://doi.org/10.1016/j.jmr.2011.12.005.
- [20] Gnahm C, Bock M, Bachert P, Semmler W, Behl NGR, Nagel AM. Iterative 3D projection reconstruction of 23Na data with an 1H MRI constraint. Magn Reson Med 2014;71:1720–32. https://doi.org/10.1002/mrm.24827.
- [21] Weingärtner S, Wetterling F, Konstandin S, Fatar M, Neumaier-Probst E, Schad LR. Scan time reduction in 23Na-magnetic resonance imaging using the chemical shift imaging sequence: evaluation of an iterative reconstruction method. Z Med Phys 2015;25:275–86. https://doi.org/10.1016/i.zemedi.2014.08.007.
- [22] Gnahm C, Nagel AM. Anatomically weighted second-order total variation reconstruction of 23Na MRI using prior information from 1H MRI. Neuroimage 2015;105:452-61. https://doi.org/10.1016/j.neuroimage.2014.11.006.
- [23] Behl NGR, Gnahm C, Bachert P, Ladd ME, Nagel AM. Three-dimensional dictionary-learning reconstruction of 23Na MRI data. Magn Reson Med 2016;75: 1605–16. https://doi.org/10.1002/mrm.25759.
- [24] Blunck Y, Kolbe SC, Moffat BA, Ordidge RJ, Cleary JO, Johnston LA. Compressed sensing effects on quantitative analysis of undersampled human brain sodium MRI. Magn Reson Med 2019;83:1025–33. https://doi.org/10.1002/mrm.27993.
- [25] Kratzer FJ, Flassbeck S, Nagel AM, Behl NGR, Knowles BR, Bachert P, et al. Sodium relaxometry using 23Na MR fingerprinting: a proof of concept. Magn Reson Med 2020;84:2577–91. https://doi.org/10.1002/mrm.28316.
- [26] Adlung A, Paschke NK, Golla AK, Bauer D, Mohamed SA, Samartzi M, et al. 23Na MRI in ischemic stroke: acquisition time reduction using postprocessing with convolutional neural networks. NMR Biomed 2021;34:e4474. https://doi.org/10.1002/nbm.4474.
- [27] Zhao Y, Guo R, Li Y, Thulborn KR, Liang ZP. High-resolution sodium imaging using anatomical and sparsity constraints for denoising and recovery of novel features. Magn Reson Med 2021;86:625–36. https://doi.org/10.1002/mrm.28767.
- [28] Kratzer FJ, Flassbeck S, Schmitter S, Wilferth T, Magill AW, Knowles BR, et al. 3D sodium (23Na) magnetic resonance fingerprinting for time-efficient relaxometric mapping. Magn Reson Med 2021;00:1–14. https://doi.org/10.1002/mrm.28873.
- [29] Lachner S, Zaric O, Utzschneider M, Minarikova L, Zbýň Š, Hensel B, et al. Compressed sensing reconstruction of 7 tesla 23Na multi-channel breast data using 1H MRI constraint. Magn Reson Imaging 2019;60:145–56. https://doi.org/ 10.1016/j.mri.2019.03.024.
- [30] Lachner S, Utzschneider M, Zaric O, Minarikova L, Ruck L, Zbýň Š, et al. Compressed sensing and the use of phased array coils in 23Na MRI: a comparison of a SENSE-based and an individually combined multi-channel reconstruction. Z Med Phys 2020;31:48–57. https://doi.org/10.1016/j.zemedi.2020.10.003.
- [31] Utzschneider M, Behl NGR, Lachner S, Gast LV, Maier A, Uder M, et al. Accelerated quantification of tissue sodium concentration in skeletal muscle tissue: quantitative capability of dictionary learning compressed sensing. Magn Reson Mater Phys Biol Med 2020;33:495–505. https://doi.org/10.1007/s10334-019-00819-2.
- [32] Utzschneider M, Müller M, Gast LV, Lachner S, Behl NGR, Maier A, et al. Towards accelerated quantitative sodium MRI at 7 T in the skeletal muscle: comparison of anisotropic acquisition- and compressed sensing techniques. Magn Reson Imaging 2021;75:72–88. https://doi.org/10.1016/j.mri.2020.09.019.
- [33] Platt T, Umathum R, Fiedler TM, Nagel AM, Bitz AK, Maier F, et al. In vivo self-gated 23Na MRI at 7 T using an oval-shaped body resonator. Magn Reson Med 2018;80:1005–19. https://doi.org/10.1002/mrm.27103.
- [34] Regnery S, Behl NGR, Platt T, Weinfurtner N, Windisch P, Deike-Hofmann K, et al. Ultra-high-field sodium MRI as biomarker for tumor extent, grade and IDH

- mutation status in glioma patients. NeuroImage Clin 2020;28:102427. https://doi.org/10.1016/j.nicl.2020.102427.
- [35] Fiege DP, Romanzetti S, Mirkes CC, Brenner D, Shah NJ. Simultaneous single-quantum and triple-quantum-filtered MRI of 23Na (SISTINA). Magn Reson Med 2013;69:1691–6. https://doi.org/10.1002/mrm.24417.
- [36] Worthoff WA, Shymanskaya A, Shah NJ. Relaxometry and quantification in simultaneously acquired single and triple quantum filtered sodium MRI. Magn Reson Med 2019;81:303–15. https://doi.org/10.1002/mrm.27387.
- [37] Pipe JG, Zwart NR, Aboussouan EA, Robison RK, Devaraj A, Johnson KO. A new design and rationale for 3D orthogonally oversampled k-space trajectories. Magn Reson Med 2011;66:1303–11. https://doi.org/10.1002/mrm.22918.
- [38] Marques JP, Kober T, Krueger G, van der Zwaag W, Van de Moortele PF, Gruetter R. MP2RAGE, a self bias-field corrected sequence for improved segmentation and T1-mapping at high field. Neuroimage 2010;49:1271–81. https://doi.org/10.1016/j.neuroimage.2009.10.002.
- [39] Rudin LI, Osher S, Fatemi E. Nonlinear total variation based noise removal algorithms. Phys D Nonlinear Phenom 1992;60:259–68. https://doi.org/10.1016/ 0167-2789(92)90242-F.
- [40] Wang Z, Bovik AC, Sheikh HR, Simoncelli EP. Image quality assessment: from error visibility to structural similarity. IEEE Trans Image Process 2004;13:600–12. https://doi.org/10.1109/TIP.2003.819861.

- [41] Fessler JA, Sutton BP. Nonuniform fast Fourier transforms using min-max interpolation. IEEE Trans Signal Process 2003;51:560–74. https://doi.org/ 10.1109/TSP.2002.807005.
- [42] Coe JI. Postmortem chemistries on human vitreous humor. Am J Clin Pathol 1969; 51:741–50. https://doi.org/10.1093/ajcp/51.6.741.
- [43] Niesporek SC, Hoffmann SH, Berger MC, Benkhedah N, Kujawa A, Bachert P, et al. Partial volume correction for in vivo 23Na-MRI data of the human brain. Neuroimage 2015;112:353–63. https://doi.org/10.1016/j. neuroimage.2015.03.025.
- [44] Wech T, Stäb D, Budich JC, Fischer A, Tran-Gia J, Hahn D, et al. Resolution evaluation of MR images reconstructed by iterative thresholding algorithms for compressed sensing. Med Phys 2012;39:4328–38. https://doi.org/10.1118/ 1.4728223.
- [45] Wang S, Su Z, Ying L, Peng X, Zhu S, Liang F, et al. Accelerating magnetic resonance imaging via deep learning. IEEE 13th Int Symp Biomed Imag 2016: 514–7. https://doi.org/10.1109/ISBI.2016.7493320.
- [46] Zimmermann M, Abbas Z, Dzieciol K, Shah NJ. Accelerated parameter mapping of multiple-Echo gradient-Echo data using model-based iterative reconstruction. IEEE Trans Med Imaging 2018;37:626–37. https://doi.org/10.1109/ TML 2012.3731504
- [47] Hu R, Kleimaier D, Malzacher M, Hoesl MAU, Paschke NK, Schad LR. X-nuclei imaging: current state, technical challenges, and future directions. J Magn Reson Imaging 2020;51:355–76. https://doi.org/10.1002/jmri.26780.